13. H. P. Zhang, A. Be'er, E.-L. Florin, H. L. Swinney, *Proc. Natl. Acad. Sci. U.S.A.* **107**, 13626 (2010).
14. T. Vicsek, A. Czirók, E. Ben-Jacob, I. Cohen, O. Shochet, *Phys. Rev. Lett.* **75**, 1226 (1995).
15. G. Grégoire, H. Chaté, *Phys. Rev. Lett.* **92**, 025702 (2004).
16. Materials and methods are available as supplementary materials on *Science* Online.
17. Y. Fily, M. C. Marchetti, *Phys. Rev. Lett.* **108**, 235702 (2012).
18. J. Deseigne, O. Dauchot, H. Chaté, *Phys. Rev. Lett.* **105**, 098001 (2010).
19. J. Anderson, *Annu. Rev. Fluid Mech.* **21**, 61 (1989).
20. L. Michaelis, M. Menten, *Biochem. Z.* **49**, 333 (1913).
21. J. Israelachvili, *Intermolecular and Surface Forces* (Elsevier, Amsterdam, 2011).
22. R. Golestanian, T. B. Liverpool, A. Ajdari, *Phys. Rev. Lett.* **94**, 220801 (2005).
23. J. Bialké, T. Speck, H. Löwen, *Phys. Rev. Lett.* **108**, 168301 (2012).
24. S. R. McCandlish, A. Baskaran, M. F. Hagan, *Soft Matter* **8**, 2527 (2012).
25. F. D. C. Farrell, M. C. Marchetti, D. Marenduzzo, J. Tailleur, *Phys. Rev. Lett.* **108**, 248101 (2012).
26. J. Tailleur, M. E. Cates, *Phys. Rev. Lett.* **100**, 218103 (2008).
27. J. Schwarz-Linek *et al.*, *Proc. Natl. Acad. Sci. U.S.A.* **109**, 4052 (2012).
28. I. Theurkauff, C. Cottin-Bizonne, J. Palacci, C. Ybert, L. Bocquet, *Phys. Rev. Lett.* **108**, 268303 (2012).

Acknowledgments: We thank J. Layné, K. Hanson, A. Grosberg, R. Dreyfus, E. Lerner, A. Baskaran, and L. Bocquet for fruitful discussions. This work was supported by the Materials Research Science and Engineering Centers program of the NSF under award number DMR-0820341 and by the U.S. Army Research Office under grant award no. W911NF-10-1-0518. We acknowledge partial support from the NASA under grant award NNX08AK04G.

Supplementary Materials

www.sciencemag.org/cgi/content/full/339/6122/936/DC1
Materials and Methods
Figs. S1 and S2
References (*29*, *30*)
Movies S1 to S6

11 September 2012; accepted 12 December 2012
10.1126/science.1230020

Global Patterns of Groundwater Table Depth

Y. Fan,[1]* H. Li,[1] G. Miguez-Macho[2]

Shallow groundwater affects terrestrial ecosystems by sustaining river base-flow and root-zone soil water in the absence of rain, but little is known about the global patterns of water table depth and where it provides vital support for land ecosystems. We present global observations of water table depth compiled from government archives and literature, and fill in data gaps and infer patterns and processes using a groundwater model forced by modern climate, terrain, and sea level. Patterns in water table depth explain patterns in wetlands at the global scale and vegetation gradients at regional and local scales. Overall, shallow groundwater influences 22 to 32% of global land area, including ~15% as groundwater-fed surface water features and 7 to 17% with the water table or its capillary fringe within plant rooting depths.

The groundwater table is an undulating surface between the oxygenated soils and the water-saturated aquifers below. Where shallow, it can influence land surface in multiple ways. For instance, shallow groundwater provides base-flow to rivers and lakes maintaining aquatic ecosystems in dry periods (*1*, *2*). Shallow groundwater tables impede drainage and create water-logged soil conditions defining wetland habitats (*2*, *3*). A shallow water table supplies root-zone soil water and photosynthetic production in droughts through capillary rise (*4*–*7*). To understand the influence of groundwater on terrestrial ecosystems, a regional and global assessment of water table depth (WTD) is required. However, WTD monitoring and reporting are highly variable across the globe and often limited to developed regions, and despite the many large-scale syntheses of groundwater conditions (*8*–*13*), there remains the lack of a global water table map.

We present global observations of WTD at 1,603,781 well sites compiled from government archives and published literature (*14*) (Fig. 1). Where government data are absent, we searched the literature for published data, which is the main source for Africa and Asia, where large data gaps still remain. The mean is shown where time series are available, but >90% of the sites have only one reading (at different times). The observed WTD varied from land surface to >200 m, but the distribution peaks at 2 to 7 m (Fig. 2). The 2- to 7-m peak reflects sampling bias; observations are made for resource monitoring where humans settle (excluding large swamps and deserts) and where the water table is lowered by pumping or drainage (figs. S1 and S2).

At first glance, there is a lack of coherent patterns; shallow WTD is found in both humid and arid climates and at both low and high elevations. However, some global trends do emerge. First, it is common for WTD to be <5 m. Second, the shallowest WTD (<0.25 m) is more common in humid climates (e.g., eastern and northern North America), pointing to some level of climate control. Third, shallow WTD is also found in arid valleys (e.g., the southwest United States), suggesting terrain-driven moisture convergence that overrides climate divisions. However, the large spatial gaps and temporal inconsistency prohibit further insights and invite a mechanistic model to elucidate the interplays among the multiple drivers at various scales.

To fill in observation gaps and infer patterns and process controls, we used a previously developed groundwater model forced by present-day climate, terrain, and sea level (*3*) (fig. S3). The model simulates vertically integrated lateral groundwater movement among grid cells at 30 arc-second (~1 km) grid spacing to resolve multiscale convergence within computational limits (*14*). We assume that, first, the permeability of continental crust drops exponentially with depth and the rate depends on land slope (*14*), so that flat valleys accumulate thick sediments (fig. S4C). Second, at any location, there is only one water table (neglecting local, perched aquifers). Third, groundwater pumping, irrigation, and drainage are not represented by the global land models providing recharge here. Thus, the model neglects local complexity and human influence and only captures the broad-scale and natural patterns that are our primary focus.

The model water table (Fig. 3) seems deeper than observations in arid regions because the observations favor valleys and oases (shallow WTD) where humans live, as seen when plotting only grid cells with observations (fig. S6). We evaluated the model by examining the residual (model-observation difference) over different continental regions (figs. S7 to S11), which suggests that the minimally simple model offers a realistic, albeit broad-scaled, sketch of global water table condition that can shed light on spatial patterns and processes.

The WTD distribution (Fig. 2) differs substantially between observations and the model results. The model suggests a much higher fraction of WTD <1 m because it includes surface water features (rivers, lakes, and inundated wetlands) fed by groundwater discharge (WTD ≤ 0) that are not sampled by wells, and few observations are in the vast boreal and interior swamps. At the deeper end, the model suggests a higher fraction of WTD > 30 m because few observations are in large deserts. The higher occurrence of observations in the 2- to 30-m range reflects observational bias.

The model offers a globally continuous but simpler (climate equilibrium, neglecting local geology) view of WTD at its natural states (without pumping or drainage). At the global scale, sea level is the dominant driver; WTD is shallow along the margins of all continents in all climates, but the ribbon of shallow WTD is wider where flat coastal plains meet the sea. This ribbon correlates well with the coastal wetlands of the world, some extending far inland across flat

[1]Department of Earth and Planetary Sciences, Rutgers University, New Brunswick, NJ 08854, USA. [2]Nonlinear Physics Group, Faculty of Physics, Universidade de Santiago de Compostela, Galicia, Spain.

*To whom correspondence should be addressed. E-mail: yingfan@rci.rutgers.edu

coastal plains and up lowland valleys. Sea-level forcing on land hydrology is well known (although not implemented in large-scale models); coastal wetlands have migrated up and down the continental shelves following sea-level change through past glacial-interglacial shifts (*3*, *15*).

At the regional scale, climate emerges as the primary driver. In mid- and low latitudes, regions of deep WTD correspond to regions of low recharge; the great deserts of the world stand out. So do the tropical swamps with high recharge (Amazon and Orinoco). In the boreal region,

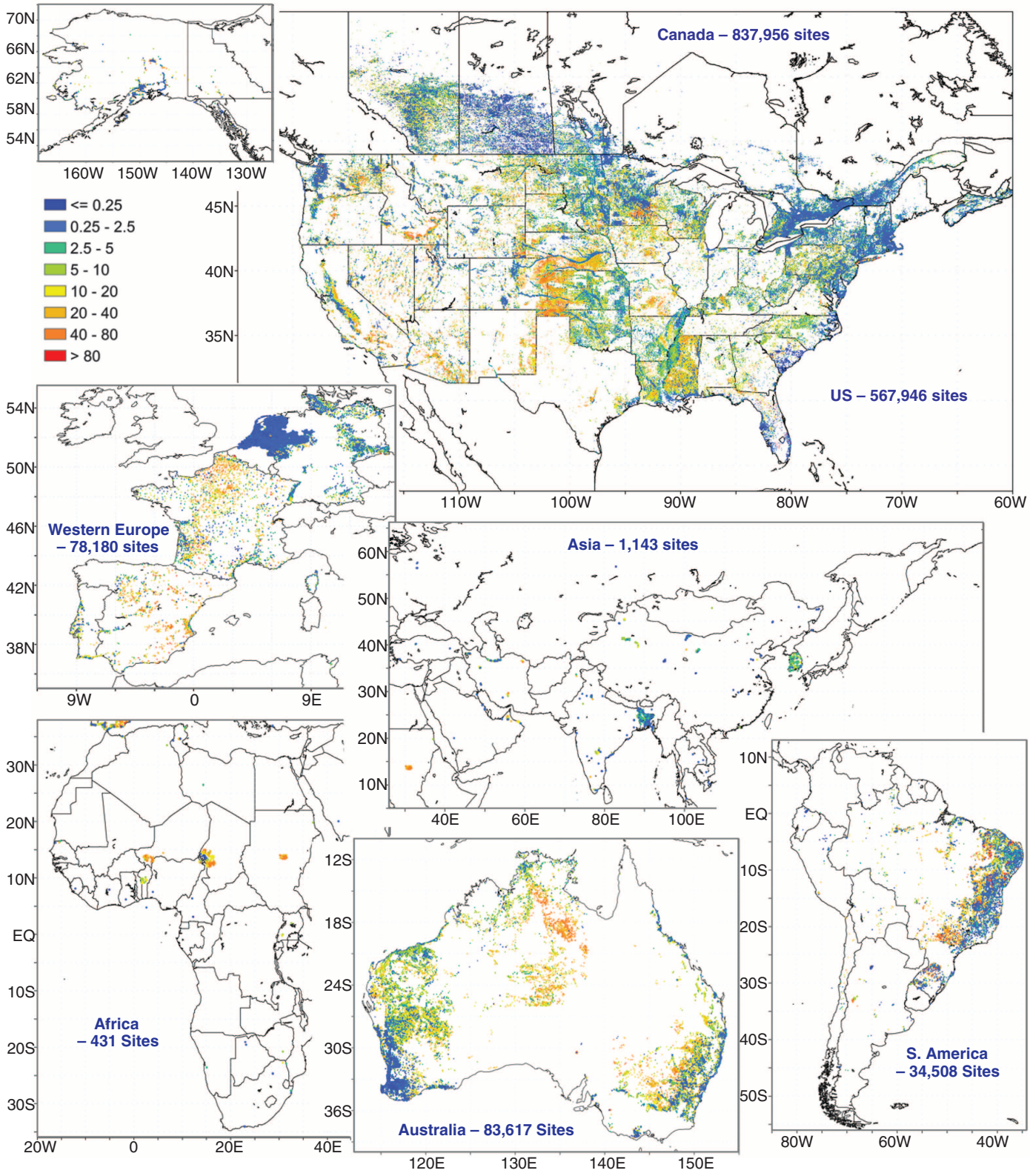

Fig. 1. Observed water table depth (m) compiled from government archives and literature (1,603,781 sites). Temporal mean is shown where time series are available.

climate control takes the form of frozen ground, where the thin thawed layer limits drainage. The large patches of shallow water table here coincide with Pan-Arctic peatlands of the world. The thin active layer is compounded by flat, low terrain, pointing to regional topographic gradient as another driver. Topographic control is also evident in warmer climates of central Amazonia and along the large swath of flat lowlands in South America from the Pantanal through the Chaco to the Pampas; large inland freshwater wetlands characterize the landscape here.

At more local scales, terrain signals dominate. Lateral convergence from high to low grounds creates a texture in WTD that overrides climate boundaries. Larger examples are arid basins where groundwater convergence from surrounding mountains maintains valley ecosystems (oases) otherwise absent (figs. S12B, S14B, and S15B). Smaller examples are river valleys etched into plateaus in semiarid climate or in humid climate with pronounced dry seasons, creating a marked gradient in water availability from valleys to ridge tops (fig. S13B). The low recharge is concentrated into a small fraction of the landscape by topography, forming discharge zones that harbor closed lakes, oases, gallery forests, and riparian wetlands, many designated as Ramsar sites of international ecological importance (table S2 and figs. S12 to S16). It is known that valleys are wetter spots and that topography is a powerful predictor of hydrologic states.

Where solar energy is not limiting, global distributions of vegetation are strongly aligned with moisture gradients indicated by annual or seasonal rainfall (*16*, *17*). However, rainfall alone cannot explain desert oases, the latter fed by groundwater due to topography-driven lateral flow that redistributes the moisture surplus or deficit across the landscape (*3*, *18*), giving patterns to WTD that defy rainfall (shallow in deserts and wide-ranging under same climate). We highlight the utility of WTD as an additional (to rainfall) moisture regulator and ecological filter with two examples, the geographic distribution of wetlands at the global scale and species differentiation and adaptation at the landscape scale.

Wetlands are habitats of vegetation adapted to water-logged soils. Small seasonal wetlands can result from local rainfall, but extensive and prolonged water-logging must be caused by shallow water tables. This is the reason that the water table map resembles the wetland map (*3*) and that the areal extents of shallow water tables and wetlands are highly correlated (fig. S17). Within a given climate regime and history, species differentiation aligns with local environmental gradients (*17*). A well-articulated gradient is the topography from valley to ridge (*19*, *20*) spanning decameters to kilometers. Because valleys are enduring features of the landscape, and because hill-to-valley groundwater convergence is slow and steady, the shallow water table in the valley offers a stable moisture source from below, creating predictable moisture gradients, particularly in dry regions or seasons. A large body of evidence suggests that WTD is a powerful niche differentiator that sorts vegetation and microbial species into anoxia-tolerant at shallow to drought-tolerant at deep water table (*5*–*7*, *19*–*29*), and for a given species, WTD regulates biomass production and drives physiological adaptation such as rooting characteristics (*6*, *30*–*34*).

The model gives a first-order estimate of global land area likely affected by shallow groundwater (*14*); ~15% is covered by lakes (excluding the large lakes in Fig. 3), rivers, and inundated wetlands fed by persistent groundwater discharge (water table rising above land surface, WTD ≤ 0), ~2% by less frequently inundated wetlands (0 < WTD ≤ 0.25 m), and 5 to 15% with WTD or its capillary fringe within the rooting depth of upland plants (*14*), adding to 22 to 32% of global land area. These results suggest a widespread and

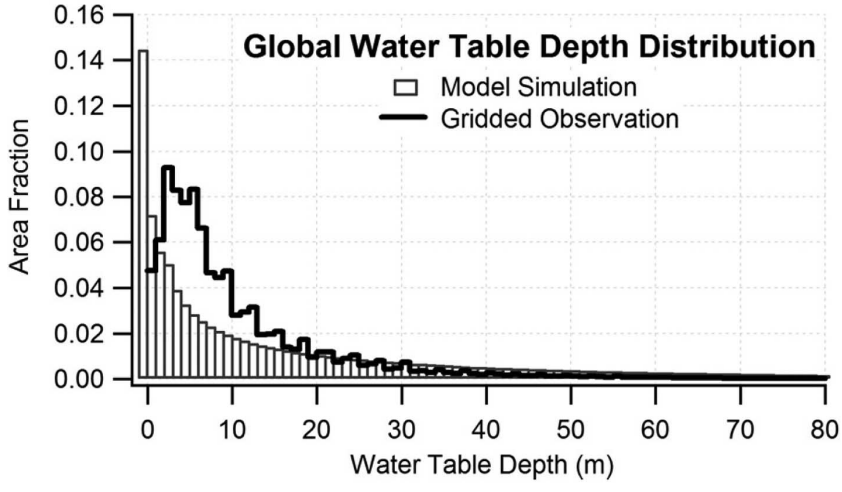

Fig. 2. Global distribution of simulated (gray) and observed (bold black) water table depth (observations first gridded into 30 arc second cells).

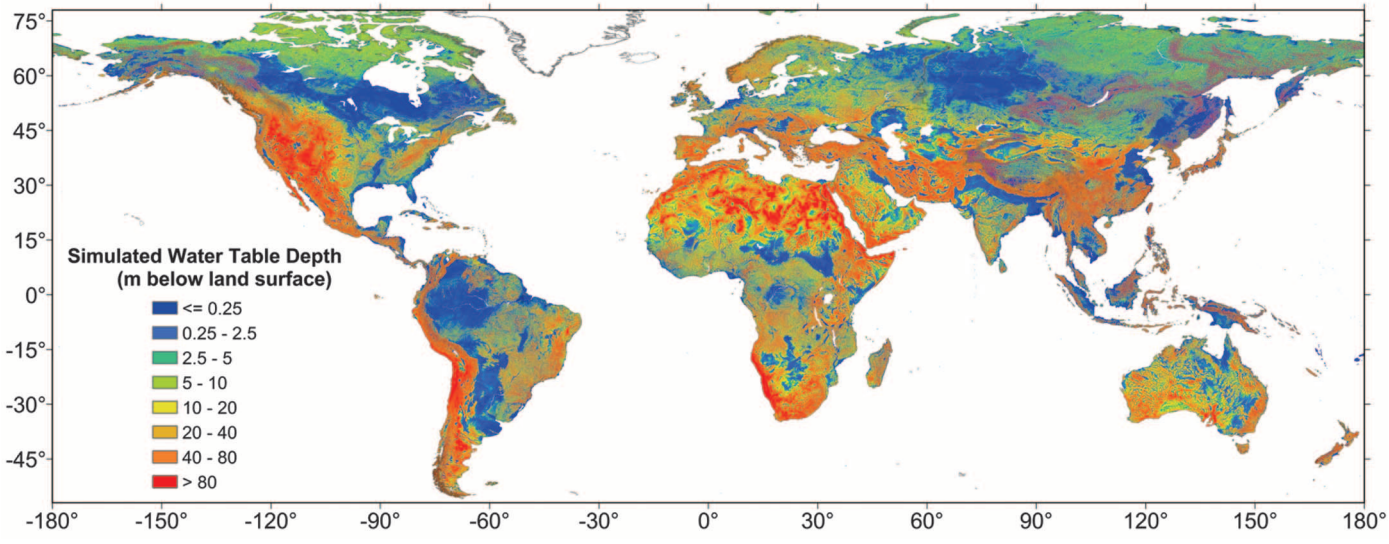

Fig. 3. Simulated water table depth (m) at 30 arc-sec grid (~1 km) constrained by observations in Fig. 1.

structured influence of groundwater on land hydrology and ecosystems and highlight the need for larger efforts to improve observing and modeling large-scale groundwater processes in the context of earth system dynamics.

References and Notes

1. T. C. Winter, J. W. Harvey, O. L. Franke, W. A. Alley, "Ground water and surface water: A single resource" (USGS Circular 1139, U.S. Government Printing Office, Denver, CO, 1998).
2. G. Miguez-Macho, Y. Fan, *J. Geophys. Res.* **117**, (D15), D15113 (2012a).
3. Y. Fan, G. Miguez-Macho, *Clim. Dyn.* **37**, 253 (2011).
4. G. Miguez-Macho, Y. Fan, *J. Geophys. Res.* **117**, (D15), D15114 (2012b).
5. D. C. Martre, D. F. Scott, C. Colvin, *Water S.A.* **25**, 137 (1999).
6. F. Orellana, P. Verma, S. P. Loheide II, E. Daly, *Rev. Geophys.* **50**, RG3003 (2012).
7. D. R. Rossatto, L. de Carvalho Ramos Silva, R. Villalobos-Vega, L. S. L. Sternberg, A. C. Franco, *Environ. Exp. Bot.* **77**, 259 (2012).
8. P. Döll, K. Fiedler, *Hydrol. Earth Syst. Sci.* **12**, 863 (2008).
9. M. Giordano, *Annu. Rev. Environ. Resour.* **34**, 153 (2009).
10. T. L. Gleeson *et al.*, *Geophys. Res. Lett.* **38**, L02401 (2011).
11. T. R. Green *et al.*, *J. Hydrol.* **405**, 532 (2011).
12. A. M. MacDonald, H. C. Bonsor, B. E. O. Docharaigh, R. G. Taylor, *Environ. Res. Lett.* **7**, 024009 (2012).
13. R. G. Taylor *et al.*, *Nat. Clim. Change* **3**, nclimate1744 (2012).
14. Materials and methods are available as supplementary material on *Science* Online.
15. H. F. Faure, R. C. Walter, D. R. Grant, *Global Planet. Change* **33**, 47 (2002).
16. B. A. Hawkins *et al.*, *Ecology* **84**, 3105 (2003).
17. H. Kreft, W. Jetz, *Proc. Natl. Acad. Sci. U.S.A.* **104**, 5925 (2007).
18. E. G. Jobbágy, M. D. Nosetto, P. E. Villagra, R. B. Jackson, *Ecol. Appl.* **21**, 678 (2011).
19. B. M. J. Engelbrecht *et al.*, *Nature* **447**, 80 (2007).
20. C. E. T. Paine, K. E. Harms, J. Ramos, *J. Trop. Ecol.* **25**, 171 (2009).
21. K. A. Dwire, J. B. Kauffman, J. E. Baham, *Wetlands* **26**, 131 (2006).
22. A. J. Elmore, J. F. Mustard, S. J. Manning, *Ecol. Appl.* **13**, 443 (2003).
23. J. Grogan, J. Galvao, *Acta Amazon.* **36**, 483 (2006).
24. F. M. R. Hughes, *J. Biogeogr.* **15**, 127 (1988).
25. S. Jirka *et al.*, *J. Veg. Sci.* **18**, 183 (2007).
26. R. Pélissier, S. Dray, D. Sabatier, *Plant Ecol.* **162**, 143 (2002).
27. M. A. Sobrado, *J. Trop. Ecol.* **26**, 215 (2010).
28. J. C. Stromberg, R. Tiller, B. Richter, *Ecol. Appl.* **6**, 113 (1996).
29. A. A. Bobrov, D. J. Charman, B. G. Warner, *Protist* **150**, 125 (1999).
30. S. K. Arndt, A. Kahmen, C. Arampatsis, M. Popp, M. Adams, *Oecologia* **141**, 385 (2004).
31. M. R. Bakker, L. Augusto, D. L. Achat, *Plant Soil* **286**, 37 (2006).
32. J. L. Carter, D. A. White, *Tree Physiol.* **29**, 1407 (2009).
33. H. S. Mishra, T. R. Rathore, V. S. Tomar, *Irrig. Sci.* **18**, 117 (1999).
34. J. Stave, G. Oba, A. B. Eriksen, I. Nordal, N. C. Stenseth, *For. Ecol. Manage.* **212**, 367 (2005).

Acknowledgments: We thank many individuals for making and providing observations (full acknowledgement is in the supplementary materials) and P. Döll for providing recharge estimates. Funding comes from U.S. National Science Foundation (NSF-AGS-1045110 and NSF-OCE-10409088), U.S. Environmental Protection Agency (EPA-STAR-RD834190), European Commission FP7 (GLOWASIS), and a Rutgers University Board of Trustees grant (651201). Computation used the Extreme Science and Engineering Discovery Environment (XSEDE) supported by U.S. National Science Foundation (NSF-OCI-1053575) and the Climate Simulation Laboratory at NCAR's Computational and Information Systems Laboratory, sponsored by the National Science Foundation and other agencies. Observations, code, and model results are accessible at https://glowasis.deltares.nl/thredds/catalog/opendap/opendap/Equilibrium_Water_Table/catalog.html.

Supplementary Materials

www.sciencemag.org/cgi/content/full/339/6122/940/DC1
Supplementary Text
Figs. S1 to S17
Tables S1 to S3
References (*35*–*228*)
Databases S1 to S3

10.1126/science.1229881

Direct Observations of Atmospheric Aerosol Nucleation

Markku Kulmala,[1]* Jenni Kontkanen,[1] Heikki Junninen,[1] Katrianne Lehtipalo,[1] Hanna E. Manninen,[1] Tuomo Nieminen,[1,14] Tuukka Petäjä,[1] Mikko Sipilä,[1] Siegfried Schobesberger,[1] Pekka Rantala,[1] Alessandro Franchin,[1] Tuija Jokinen,[1] Emma Järvinen,[1] Mikko Äijälä,[1] Juha Kangasluoma,[1] Jani Hakala,[1] Pasi P. Aalto,[1] Pauli Paasonen,[1] Jyri Mikkilä,[2] Joonas Vanhanen,[2] Juho Aalto,[3] Hannele Hakola,[4] Ulla Makkonen,[4] Taina Ruuskanen,[1] Roy L. Mauldin III,[1,5] Jonathan Duplissy,[1] Hanna Vehkamäki,[1] Jaana Bäck,[6] Aki Kortelainen,[7] Ilona Riipinen,[8] Theo Kurtén,[1,9] Murray V. Johnston,[10] James N. Smith,[7,11] Mikael Ehn,[1,12] Thomas F. Mentel,[12] Kari E. J. Lehtinen,[4,7] Ari Laaksonen,[4,7] Veli-Matti Kerminen,[1] Douglas R. Worsnop[1,4,7,13]

Atmospheric nucleation is the dominant source of aerosol particles in the global atmosphere and an important player in aerosol climatic effects. The key steps of this process occur in the sub–2-nanometer (nm) size range, in which direct size-segregated observations have not been possible until very recently. Here, we present detailed observations of atmospheric nanoparticles and clusters down to 1-nm mobility diameter. We identified three separate size regimes below 2-nm diameter that build up a physically, chemically, and dynamically consistent framework on atmospheric nucleation—more specifically, aerosol formation via neutral pathways. Our findings emphasize the important role of organic compounds in atmospheric aerosol formation, subsequent aerosol growth, radiative forcing and associated feedbacks between biogenic emissions, clouds, and climate.

Atmospheric aerosol formation [that is, the formation of molecular clusters and their growth to larger sizes (*1*, *2*)] has an important effect on aerosol particle number concentrations (*3*, *4*) and on climate through indirect radiative effects (*5*, *6*). To understand the initial steps of atmospheric aerosol formation, one must have detailed knowledge of the concentrations of neutral and charged clusters, their chemical composition, and gaseous compounds participating in their formation and growth. However, size-segregated measurements of sub–2-nm clusters are extremely rare, and until now, no one has taken comprehensive and simultaneous field measurements of charged and neutral clusters and their precursors (supplementary materials, section 3).

Recent technical developments make it possible to measure the concentrations and size distributions of ions, molecular clusters, and nanoparticles in the 1- to 2-nm mobility diameter range and to simultaneously obtain information about the chemical composition of these entities and their interactions with trace gases. Here, we present a comprehensive analysis of such measurements, conducted between 14 March and 16 May 2011, at the SMEAR II station (*7*) in Hyytiälä, southern Finland. We measured the total nanoparticle and ion concentrations, along with the concentrations of gaseous compounds, including sulfuric acid, volatile organic compounds, ammonia, amines, ozone, sulfur dioxide, and nitrogen oxides. The instruments we used to take our measurements are described in greater detail in the supplementary materials (sections 1.3.1 to 1.3.7).

We categorized each day of the measurement campaign as a "nucleation event day," a "non-event day," or an "undefined day" (table S7) (*8*). We determined the concentrations of nanoparticles and ions separately for six size classes between 0.9 and 2.1 nm (supplementary materials, section 1.2). For each size class, we calculated the concentration of nanoparticles originating from neutral formation pathways, N_n, from the relation $N_{tot} = N_{ions} + N_{rec} + N_n$, where N_{tot} is the total measured nanoparticle concentration in that size class, N_{ions} is the corresponding ion concentration, and N_{rec} is the estimated concentration of neutral particles originating from the recombination of

[1]Department of Physics, University of Helsinki, Finland. [2]Airmodus Oy, Helsinki, Finland. [3]SMEAR Station II, Hyytiälä, Finland. [4]Finnish Meteorological Institute, Finland. [5]University of Colorado at Boulder, Boulder, CO, USA. [6]Department of Forest Sciences, University of Helsinki, Finland. [7]University of Eastern Finland, Kuopio, Finland. [8]University of Stockholm, Stockholm, Sweden. [9]Department of Chemistry, University of Helsinki, Finland. [10]University of Delaware, Newark, DE, USA. [11]National Center for Atmospheric Research, Boulder, CO, USA. [12]Forschungszentrum Juelich, IEK-8, 52425 Juelich, Germany. [13]Aerodyne Research, Billerica, MA, USA. [14]Helsinki Institute of Physics, Helsinki, Finland.

*To whom correspondence should be addressed. E-mail: markku.kulmala@helsinki.fi